



Real time tracing of valence-shell electronic coherences with attosecond transient absorption spectroscopy

A. Wirth^a, R. Santra^{b,c}, E. Goulielmakis^{a,*}

^a Max-Planck-Institut für Quantenoptik, Hans-Kopfermann-Str. 1, D-85748 Garching, Germany

^b Center for Free-Electron Laser Science, DESY, Notkestrasse 85, 22607 Hamburg, Germany

^c Department of Physics, University of Hamburg, Jungiusstrasse 9, 20355 Hamburg, Germany

ARTICLE INFO

Article history:

Available online 15 June 2012

Keywords:

Attosecond transient absorption Spectroscopy
Electron density
Valence electron motion
Optical attosecond streak camera
Charge state time-resolved ionization of atoms
Ionization of atoms
Valence-shell electron dynamics
Spin-orbit dynamics
Krypton
Xenon
Quasi-monocycle laser pulses
Attosecond spectroscopy
Attosecond physics
Attosecond EUV pulses
Attosecond XUV pulses
Reconstruction of valence electron density
Valence shell
Electronic coherences
Ionization dynamics
Sub-cycle delay
Hole-hole correlations

ABSTRACT

The chemical properties of atoms, molecules and of more complex systems such as clusters, nanoparticles or condensed matter systems are determined by valence electrons. Real-time control of these properties requires the capability of tracing as well as of driving valence electrons on their native temporal scale of motion, that is, within tens to thousands of attoseconds. Here we detail the technique of attosecond transient absorption spectroscopy. It combines the extreme sensitivity of core-level spectroscopy with the unprecedented temporal resolution offered by the tools of attosecond technology. We use the technique to demonstrate real-time tracing and complete characterization of coherent electron motion triggered by single, double or multiple ionization of atoms exposed to intense, few-cycle pulses. Our work opens the door to high fidelity, time-domain studies and control of electron dynamics in the microcosm.

© 2012 Elsevier B.V. All rights reserved.

1. Introduction

Progress in light technology over the last decade has widened the scope of ultrafast science to include tracing and real-time control of electronic dynamics [1,2] in atoms, molecules and condensed matter. Field control of intense few-cycle waveforms has enabled the reproducible generation of isolated extreme ultraviolet (EUV) attosecond pulses [3] and the establishment of novel methods for chronoscopy, such as the attosecond streak camera [4–9]. Owing to their unprecedented resolution [10,11], these tools have made possible the real-time tracing of ultrafast electron wavepackets and associated dynamics, triggered by direct or indirect pho-

toionization (e.g. Auger decay) of atoms [12], molecules [13] and condensed matter [14].

Valence electron motion can be initiated by the coherent population of valence electronic state manifolds of virtually any microscopic system—from a single atom to a complex protein—and results in the dynamic evolution of its electronic charge distribution. Because the chemical reactivity of atoms and molecules is closely linked to their electronic charge distributions [15], measurement and control of electron dynamics can open up new ways for steering chemical reactions on extreme time scales. Electron motion in atoms [16] or in molecules [13] has been recently accessed via bound and free wavepacket interferences, harmonic interferometry as well as angularly resolved ion momentum spectroscopy [17–19]. Here we demonstrate a more generic probe scheme with attosecond temporal resolution as well as broad

* Corresponding author.

E-mail address: elgo@mpq.mpg.de (E. Goulielmakis).

dynamic range, capable to capture valence dynamics unfolding within tens of attoseconds or hundreds of femtoseconds, offering new possibilities for tracing electronic processes in complex molecular systems [20].

2. Attosecond transient absorption spectroscopy

2.1. The concept

Our approach is based on the well-established approach for probing structural changes at the valence shell of atoms, molecules or solids, namely the technique of core-level X-ray absorption spectroscopy [21–23]. Implemented with extreme ultraviolet pulses generated via high harmonic generation (HHG)—typically of femtosecond duration—this technique has been successfully employed to trace structural dynamics in solids [24], as well as the quantum-state resolved ionization of atoms [25] and molecules [26] triggered by femtosecond pulses in the NIR. Here we show that this technique can be endowed with attosecond resolution by employing EUV attosecond pulses to probe ultrafast electron dynamics initiated by a precisely controlled few-cycle light waveform. Variations of this technique, in the meanwhile implemented by other groups, have allowed access to the autoionization of atoms [27] as well as to the interference of transiently bound electron wave packets [28].

Fig. 1 illustrates triggering and probing of electron dynamics within the concept of attosecond transient absorption spectroscopy. An intense few-cycle laser pulse (red) liberates electrons from the $4p$ valence shell of krypton atoms to create singly, doubly or triply charged ions in the $4p^{-1}$, $4p^{-2}$ and $4p^{-3}$ manifolds of quantum states. An EUV pulse (purple) can promote the generated ions to the core-hole excited-state manifolds $3d^{-1}$, $3d^{-1}4p^{-1}$ and $3d^{-1}4p^{-2}$. Inner shell excitation is typically followed by Auger decay of the core-hole states. If the EUV pulse is transmitted through an ensemble of ionic specimen, resonant absorption will occur and will be manifested by sharp dips in the transmitted spectrum centered at the energy of the characteristic transitions of the ion. The linewidth is inversely proportional to the core-hole life time of the system. For krypton ions, the $3d$ Auger decay is on the order of $T_{3d} \sim 7$ fs resulting in line widths of ~ 88 meV [29]. In close analogy to femtosecond transient absorption spectroscopy, pioneered by Mathies and coworkers [30–33], quantum state populations as

well as coherent dynamics of the studied systems are imprinted on sample-transmitted spectra of the probe pulse that can be recorded as function of the pump–probe delay between the two pulses.

2.2. Basic instrumentation and the optical attosecond streak camera

The experimental setup used to supplement absorption spectroscopy with attosecond resolution is detailed in Fig. 2(a). Waveform reproducible quasi-monocycle laser pulses are focused ($f = 50$ cm) into a neon filled (~ 220 mbar) quasi-static gas cell to generate EUV pulses via the process of high harmonic generation [34]. The emerging, highly collimated EUV pulses are transmitted through a disc-like Zirconium (Zr) foil (150 nm) mounted on a thin pellicle (15 μm), while the near infrared (NIR) pulses—which are also making their way through the Ne cell—are transmitted around the margins of the Zr disc to create an annular beam. A module, comprised of a concave, multilayer-coated inner mirror and a silver coated concave annular sector (outer mirror), focuses ($f = 12.5$ cm) EUV and NIR fields into a Ne gas jet for streaking experiments or a quasi-static cell for transient absorption experiments (Kr or Xe for the experiments presented here). Streaking spectrograms recorded by this apparatus [8] allow not only the precise temporal characterization of the NIR electric field [6], but also the reconstruction of the EUV pulse characteristics utilizing a FROG based retrieval [35,36]. The intensity profile of an attosecond EUV pulse measured by the apparatus is displayed in Fig. 2(b).

The gas cell—used for transient absorption measurements—has diameter of < 1.0 mm, substantially smaller than the > 3 mm confocal parameter of the focused laser beam. The required gas density in the quasi-static gas cell for recording transient absorption spectra depends on the EUV photoabsorption cross-section. To quote a few useful numbers, a cross section of ~ 1 Mb and an atom density of $2.5 \cdot 10^{18}$ atoms/cm³ (~ 100 mbar), yields an EUV absorption of $> 20\%$ within the bandwidth of an absorption line. The estimation suggests robust signals which are essential for high fidelity measurements.

The transmitted attosecond pulse is focused by a concave mirror (ROC = -340 mm), placed at nearly grazing incidence ($\sim 64^\circ$) with respect to the incident beam, to create a vertical focus on the plane of the entrance slit of an EUV spectrometer. The spectrometer which is based on the Rowland-circle geometry, utilizes a ~ 2400 lines/mm concave grating to spectrally disperse the EUV beam on a single-stage microchannel plate (cesium iodide coated photocathode) followed by a phosphor screen and fiber-coupled, peltier-cooled CCD camera. We obtain a spectral resolution better than 350 meV at ~ 80 eV.

3. Charge state time-resolved ionization of atoms

One of the first experiments [37] that employed picoseconds EUV transient absorption on NIR strong-field generated ions aimed at the retrieval of the EUV pulse width by using the ionization via a strong field as the probe. With attosecond EUV probes considerably shorter than the NIR driver pulse, the technique affords access into the dynamics of strong field ionization and the accurate determination of the ionization gate which is the key parameter for affecting or even controlling the coherence of the ensuing electron dynamics in the valence shell, to be discussed in the next sections. Ionization dynamics can be elucidated by tracing absorption of an attosecond pulse in the presence of the strong field, namely within the time span where both pump and probe pulses overlap. The quantity that links the population of the absorbing species to the experimentally recorded signals is absorbance and is defined as: $A(E, \tau) = \ln(I_0(E, \tau)/I_{\text{trans}}(E, \tau))$, where $I_0(E, \tau)$ is the spectral density

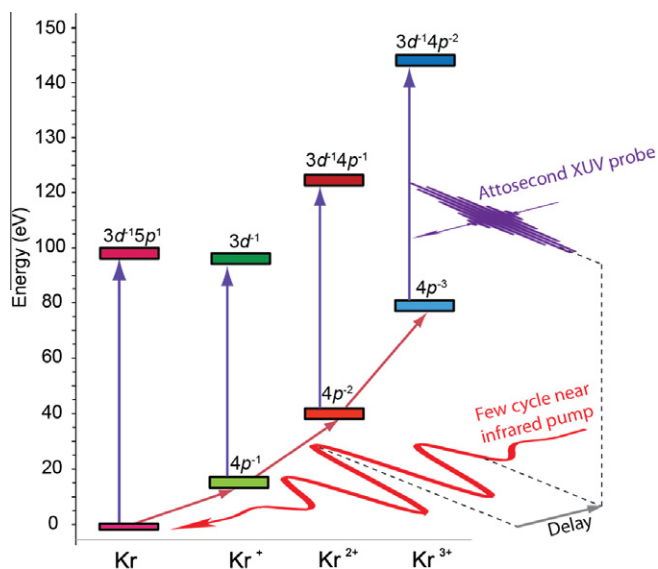


Fig. 1. Probing krypton atoms and ions by attosecond absorption spectroscopy.

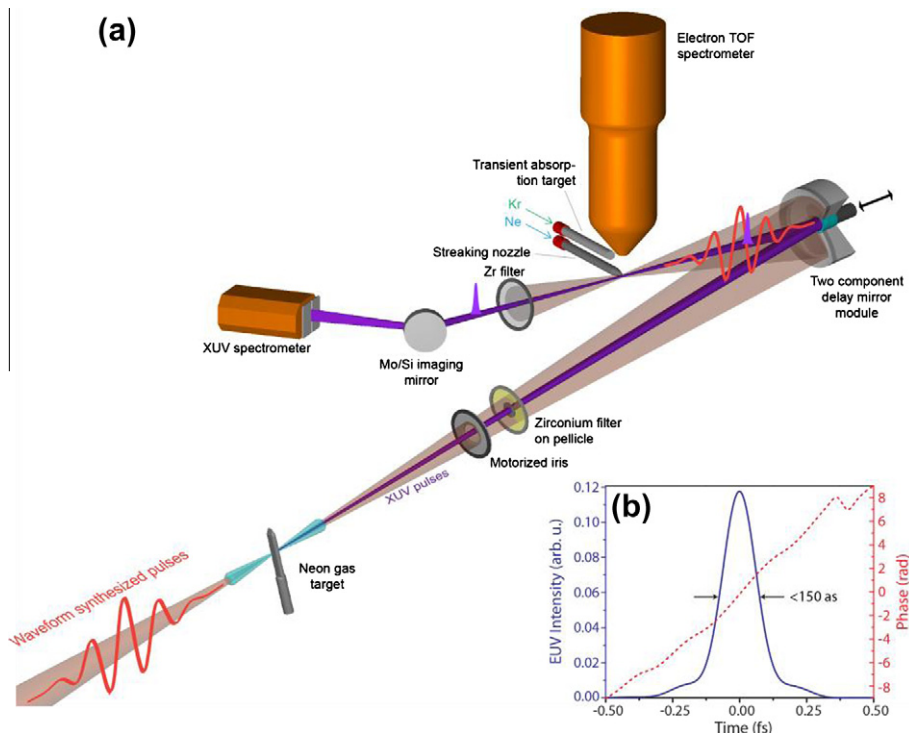


Fig. 2. (a) Schematic of the experimental set-up for attosecond streaking and attosecond transient absorption experiments. (b) Attosecond EUV pulse intensity profile retrieved by attosecond streaking.

recorded at the outermost negative delay (here at -11 fs), i.e. when the EUV probe proceeds the ionizing laser pulse in the atomic sample, and $I_{\text{trans}}(E, \tau)$ the spectral density recorded at a pump–probe delay τ . This relation is precisely linear if the EUV probe and the pump pulse are not temporally overlapping. In the case of the temporal overlap the strong, pump field—depending on its strength—can perturb the oscillating dipole induced by the EUV pulse giving rise to more complex absorption dynamics [38]. Absorption spectra recorded for different delays (absorption spectrogram) between the NIR pump and sub-fs probe pulse are displayed in Fig. 3. The shown spectrogram is averaged over 17 consecutive scans with a delay step of 200 as taken at an NIR intensity of $(6.8 \pm 1.1) \cdot 10^{14}$ W/cm 2 . Whereas for neutral atomic species databases can be used to assign transitions to EUV absorption spectra, the absorption of ionic species is not equally well studied. For the needs of the presented work, dipole spectra for various charge states and therewith absorption spectra have therefore been calculated by the COWAN atomic structure code [39,40]. In particular we have calculated the statistically weighted oscillator strength gf of dipole allowed EUV $3d \rightarrow 4p$ transitions for $\text{Kr}^+(4p^{-1})$, $\text{Kr}^{2+}(4p^{-2})$ and $\text{Kr}^{3+}(4p^{-3})$ in order to reproduce the spectra of Fig. 3. For every charge state ($i = 1, 2, 3$) the atomic structure code provides all dipole allowed oscillator strengths $gf_n^{(i+)}$ and corresponding transition energies $\omega_n^{(i+)}$. The expected absorption cross-section $\sigma(\omega)^{(i+)}$ is calculated as:

$$\begin{aligned} \sigma(\omega)^{(i+)} &\propto G(\omega) * \sum_n gf_n^{(i+)} L_n(\omega) \\ &\propto \sqrt{\frac{4 \ln(2)}{\pi \Delta^2}} e^{-\frac{4 \ln(2)(\omega - \omega_0)^2}{\Delta^2}} * \sum_n gf_n^{(i+)} \frac{1/(2\pi)\Gamma_n}{(\omega - \omega_n^{(i+)} + \omega_{\text{off}}^{(i+)})^2 + (\Gamma_n/2)^2} \end{aligned}$$

where the convolution (displayed as $*$) of the sum of Lorentzian line shape functions $L_n(\omega)$ with the normalized Gauss function $G(\omega)$ accounts for the finite spectrometer resolution. The spectrometer resolution Δ had been 0.31 eV for the particular data set shown in

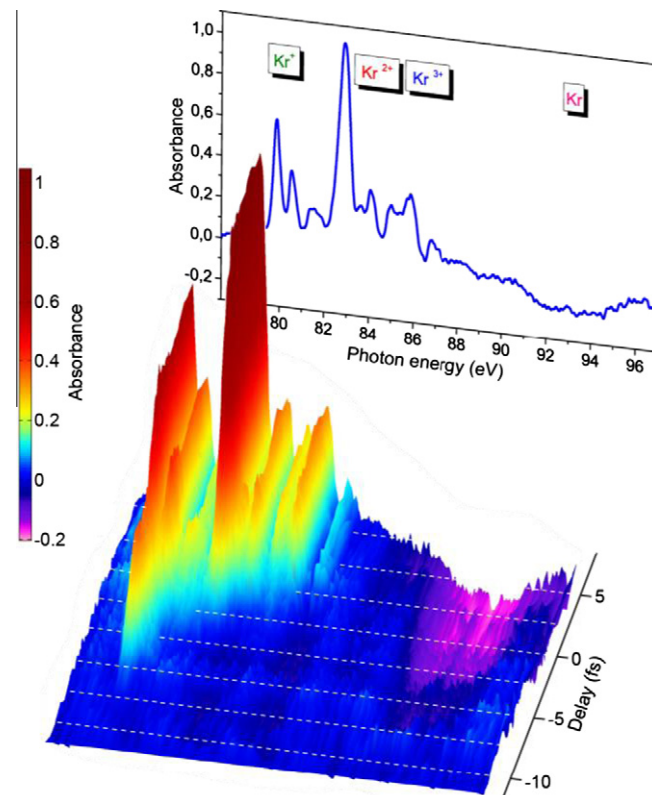


Fig. 3. High resolution EUV transient absorption spectrogram of krypton ions. An EUV attosecond pulse tracks the formation of charge states up to Kr^{3+} by a ~ 3.8 fs long NIR pulse at an intensity of $(6.8 \pm 1.1) \cdot 10^{14}$ W/cm 2 and the pertaining depletion of neutral atoms as a function of pump–probe delay. The absorption spectrum displayed in the background was sampled at a delay of 8.5 fs.

Fig. 3 and we assume a charge state and j -independent decay width Γ_n of the $3d^{-1}$ hole of 88 meV [29]. To account for the limited accuracy in the absolute energy calibration of our spectrometer (~ 0.5 eV) as well as for inaccuracies of the atomic structure code, we have introduced the fitting parameter $\omega_{\text{off}}^{(i+)}$ which allows for an overall shift of the absorption pattern along the energy axis ($\omega_{\text{off}}^{(1+)} = 0.65$ eV, $\omega_{\text{off}}^{(2+)} = 1.3$ eV, $\omega_{\text{off}}^{(3+)} = 1.35$ eV). The three fit parameters were chosen to minimize the fitting error. The absorption cross section obtained for the various Kr charge states are contrasted with experimental data in Fig. 4 and suggest that our broadband EUV probe is able to track the formation of charge states up to Kr^{3+} .

Having assigned absorption lines to charge states we comment now on Fig. 3. Disregarding a forerunner in the main Kr^+ lines of Fig. 3, the origin of which is still unclear, the Kr^{2+} lines appear with a well resolved delay after the Kr^+ lines. Furthermore, the formation of the Kr^{3+} lines appears delayed with respect to that of the Kr^{2+} ones. While the absorption—and therewith the population of ions—is building up with increasing delay, the population of the neutral atoms is reduced which leads to a negative broadband absorption in the range of 90–95 eV. This is the spectral range in which neutral krypton yields three major absorption lines at ~ 91.2 , ~ 92.4 and at 92.6 eV corresponding to the $3d_{5/2}^{-1}5p$, $3d_{3/2}^{-1}5p$, $3d_{3/2}^{-1}6p$ and the $3d_{5/2}^{-1}6p$ resonance [41]. The severe broadening of the discrete absorption lines to yield the observed wideband absorption can be attributed to strong NIR perturbation of the absorbing EUV dipole response [38,42].

4. Tracing valence-shell electron dynamics

4.1. Launching and tracing spin-orbit dynamics in singly ionized Kr atoms

Modern experiments suggest that strong laser field ionization populates not only the ground state but also excited states of the generated ions [25,43–45]. A demonstrative explanation for this observation is that an ultrashort strong laser pulse tunnel-ionizes all noble gas atoms (excluding helium) by pulling an electron out of the valence p_z orbital, where z indicates the laser polarization

axis. With a hole in its valence p_z orbital, such an ion is not anymore in an eigenstate but rather in a superposition of different quantum states [46]. A critical question is whether these superposition states are being populated coherently during strong-field ionization to allow the creation of subsequent wavepacket motion in the valence shell of the generated ion.

The experimental scheme used to shed light on this question is summarized in Fig. 5(a). Attosecond EUV pulses centered at 80 eV probe the valence shell of the singly ionized Kr atom (see also spectra in Fig. 4) via three dipole allowed EUV transitions, manifested by three absorption lines in the EUV spectrum. They can be attributed to the $4p_{3/2}^{-1} \rightarrow 3d_{5/2}^{-1}$ (~ 79.8 eV), $4p_{1/2}^{-1} \rightarrow 3d_{3/2}^{-1}$ (~ 80.4 eV) and $4p_{3/2}^{-1} \rightarrow 3d_{3/2}^{-1}$ (81.1 eV) transition as suggested by the Kr^+ energy diagram in Fig. 5(a). The given transition energies are calculated using the multiconfiguration Dirac-Fock program package GRASP92 [47]. The energy level diagram shows the spin-orbit splitting of the $4p$ and $3d$ subshells. The $4p_{j=3/2}^{-1}$ ground state and the $4p_{j=1/2}^{-1}$ excited state manifolds, comprising four ($m_{j=3/2} = \pm 3/2, \pm 1/2$) and two ($m_{j=3/2} = \pm 1/2$) states, respectively (j denotes the total angular momentum; m_j its projection on the z axis being lined up with the laser polarization axis as indicated in the inset of Fig. 5(a)) are separated energetically by 0.67 eV [48]. The presence of all three absorption lines in our attosecond absorption spectrograms suggests indeed that both the ground and first excited levels are populated by strong-field ionization. Coherences between the two levels can be probed via the simple Λ -scheme $4p_{1/2}^{-1} \rightarrow 3d_{3/2}^{-1} \leftarrow 4p_{3/2}^{-1}$.

To address the question of whether a strong field generates coherent superpositions in the valence shell as well as to enable a direct comparison with the presented experimental results, we have performed ab initio modeling of the interaction of Kr atoms with a strong laser field for the experimental parameters as described in detail in [46]. Solving the time-dependent Schrödinger equation for a quasi monocycle ionizing NIR field, linearly polarized along the quantization axis, has yielded the evolution of the density matrix elements during the ionization process [49] and their final values after the ionization process which amount to relative populations of $\rho_{3/2,3/2}^{(\pm 1/2)} = 0.69$, $\rho_{1/2,1/2}^{(\pm 1/2)} = 0.26$, and $\rho_{3/2,3/2}^{(\pm 3/2)} = 0.05$. We have assumed a 3.8 fs laser pulse with sinusoidal waveform, centered at 750 nm at an intensity of $\sim 3 \cdot 10^{14}$ W/

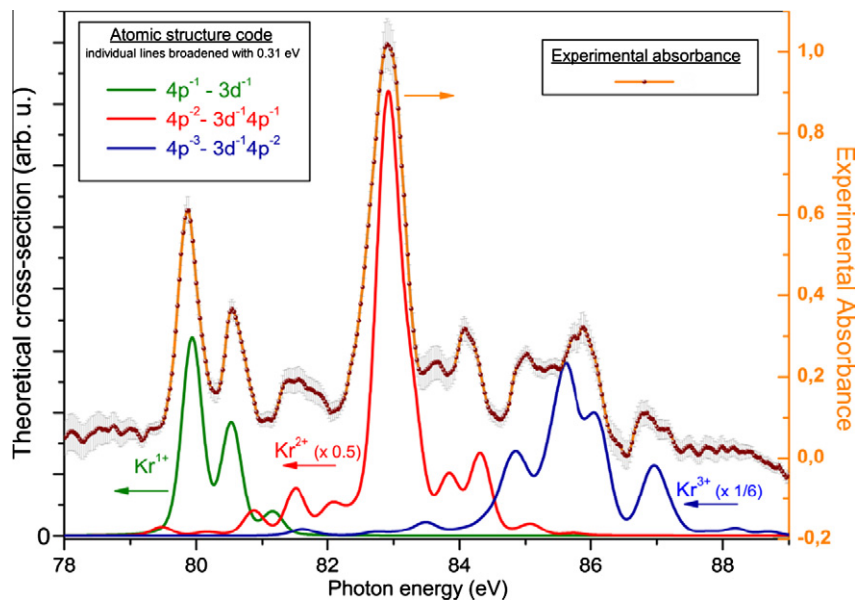


Fig. 4. Assignment of absorption lines to atomic charge states of krypton. Experimental transient absorption spectrum recorded at a delay of 8.5 fs (see Fig. 3) (red dots, connected by orange line) is compared to calculated absorption cross-section for EUV radiation of Kr^+ , Kr^{2+} and Kr^{3+} (see text for details). (For interpretation of the references to color in this figure legend, the reader is referred to the web version of this article.)

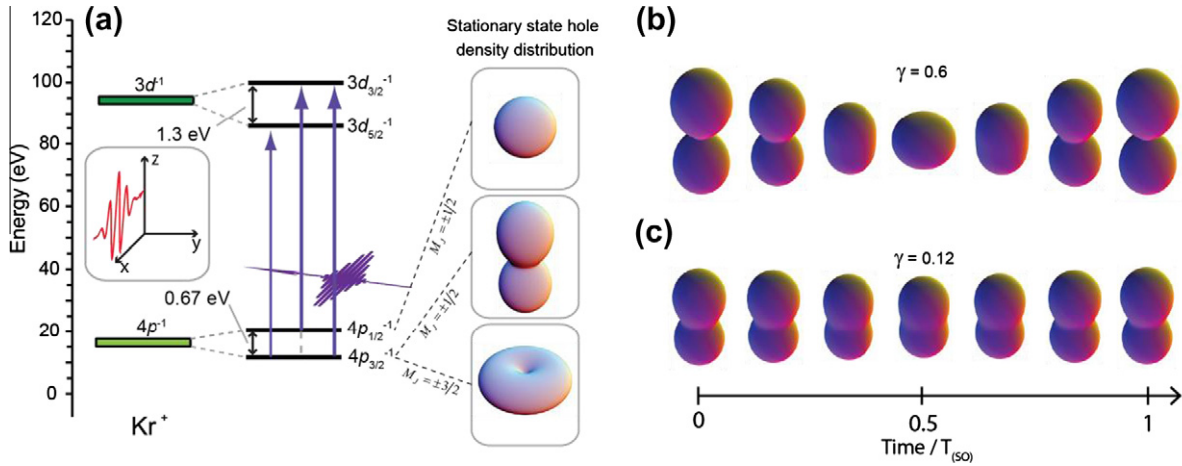


Fig. 5. Attosecond EUV probing scheme of states and valence shell dynamics in Kr^+ . (a) Energy level diagram of krypton singly charged ions showing the spin-orbit splitting of the $4p$ and $3d$ subshells. The three insets on the right display the stationary state hole density distribution of the corresponding orbitals of the $4p$ subshell depending on the magnetic projection quantum number M_j , where the polarization of the ionizing NIR laser pulse is assumed to be aligned along the vertical axis (see inset). Panels (b) and (c) show the evolution of the ensemble-averaged angular hole density distributions in the $4p$ subshell of Kr^+ based on an ab initio simulation of strong-field ionization over one complete wavepacket period T_{so} for two different NIR pulse durations. An ionizing pulse with a duration of ~ 3.8 fs yields a coherent electron motion with a degree of coherence of 0.6 (b) and a 7.6 fs long pulse a degree of coherence of only 0.12 (c).

cm^2 . The hole populations have been normalized such that the trace of the reduced density matrix at 10 fs (after the peak of the pulse) equals one. Angular contributions of the stationary hole density distribution of the corresponding orbitals of the $4p$ subshell are depicted in Fig. 5(a).

Only states with the same value of m_j can form a coherent superposition characterized with a non-zero value of the corresponding off-diagonal element of the density matrix. For Kr^+ this condition is fulfilled by the $4p_{3/2}^{-1}$, $m = \pm 1/2$ and $4p_{1/2}^{-1}$, $m = \pm 1/2$ states, respectively. The degree of coherence between these states can be characterized by the parameter

$$\gamma(t) = \frac{|\rho_{3/2,1/2}^{(1/2)}(t)|}{\sqrt{\rho_{3/2,3/2}^{(1/2)}(t) \cdot \rho_{1/2,1/2}^{(1/2)}(t)}}$$

which normalizes $|\rho_{3/2,1/2}^{(1/2)}(t)|$ with the pure state coherence $\sqrt{\rho_{3/2,3/2}^{(1/2)}(t) \cdot \rho_{1/2,1/2}^{(1/2)}(t)}$. Perfect coherence corresponds to $\gamma = 1$, whereas incoherent superpositions yield $\gamma = 0$.

Fig. 5(b) shows predicted ensemble-averaged hole density distributions for one full spin-orbit period amounting to $T_{\text{so}} \approx 6.2$ fs for $\gamma = 0.6$ which is contrasted with the expected motion being triggered with a 7.6 fs long laser pulse, creating a coherent superposition yielding only a degree of coherence of ~ 0.12 (Fig. 5(c)) resulting in a dramatic decrease of the contrast of the evolving spin-orbit wavepacket. This clearly demonstrates that confinement of the ionization to a fraction of the wavepacket period is essential to trigger highly coherent electron motion with a strong field. Our quasi monocycle pulses fulfill this prerequisite of exerting a short enough trigger event.

By conducting attosecond absorption measurements over several tens of femtoseconds following the formation of the ions via the strong NIR field, complete reconstruction of the valence electron motion in Kr^+ becomes possible. The generated coherence and therewith the temporal variation of the relative phase between the valence shell states $4p_{j=1/2}^{-1}$ and $4p_{j=3/2}^{-1}$ translate into a pronounced modulation of the observed absorption strength as a function of pump-probe delay for the $4p_{1/2}^{-1} \rightarrow 3d_{3/2}^{-1}$ and $4p_{3/2}^{-1} \rightarrow 3d_{3/2}^{-1}$ transitions (Fig. 6(a)). A scan is obtained at $(3.1 \pm 0.5) \cdot 10^{14} \text{ W/cm}^2$, recording the absorbance over an extended time range at a sampling resolution of 1 fs and including a delay range (14.1–24.0 fs) where the sampling resolution has

been increased to 0.3 fs. The pressure in the gas cell was ~ 80 mbar. The observed periodicity of the modulation of 6.2 fs is in good agreement with the energy spacing of 0.67 eV mentioned earlier. The modulation is most pronounced in the weaker $4p_{3/2}^{-1} \rightarrow 3d_{5/2}^{-1}$ transition and is absent from the $4p_{3/2}^{-1} \rightarrow 3d_{5/2}^{-1}$ transition, which is insensitive to the quantum superposition because the $4p_{1/2}^{-1} \rightarrow 3d_{5/2}^{-1}$ transition is electric dipole forbidden.

4.2. Reconstruction of valence electron density

The absorption spectrogram shown in Fig. 6(a) was obtained by averaging over several, here 4, consecutive scans, all taken under the same experimental conditions. All EUV spectra of the combined spectrogram were normalized in the spectral range from 75.7 to 77.1 eV (i.e. the low energy side next to the Kr^+ absorption lines) to reduce noise originating from flux variations of the EUV probe pulse. The absorbance $A(\omega, \tau)$, at the outermost negative delay has been used as a reference spectrum. To reconstruct the Kr^+ quantum state distribution, the coherence of the spin-orbit wavepacket motion as well as the quantum phase, a fit to the experimental data is performed using the model equation

$$A(\omega, \tau) = -\ln[\exp[-n_0 \sigma(\omega, \tau)L] * G(\omega)] + A_0 \quad (1)$$

Here, $\sigma(\omega, \tau)$ is an analytical description of the cross-section of the three absorption lines of Kr^+ based on Eq. (35) in [50]. Furthermore, τ indicates the time of probing, $n_0 = 2 \cdot 10^{18} \text{ cm}^{-3}$ the initial number density of neutral atoms, $L = 1.0$ mm the length of the target cell and $G(\omega)$ an area-normalized Gaussian convolution function with Δ being the FWHM value characterizing the finite spectrometer resolution and A_0 a constant offset. The coherence term in $\sigma(\omega, \tau)$ is described by $\rho_{3/2,1/2}^{(1/2)}(\tau) = |\rho_{3/2,1/2}^{(1/2)}| \exp(i\phi_{\text{so}}(\tau)) = |\rho_{3/2,1/2}^{(1/2)}| \exp(i\Delta E_{\text{so}}\tau + i\delta)$, where ΔE_{so} is the spin-orbit wavepacket splitting and δ is a phase offset which depends on the choice of the time origin $\tau = 0$ (atomic units $\hbar = e = m_e = a_0 = 1$ are used). We have chosen $\tau = 0$ such that it coincides with the 95% value of the absorbance strength of the $4p_{3/2}^{-1} \rightarrow 3d_{5/2}^{-1}$ transition. Hence, for a sufficiently short pump pulse that confines ionization on much smaller time-scales than the wavepacket period—for instance the sub-optical cycle light field transient as used in [38]—it is meaningful to choose $\tau = 0$ such that it coincides with the maximum of the instantaneous intensity of the synthesized light field transient. In this case the

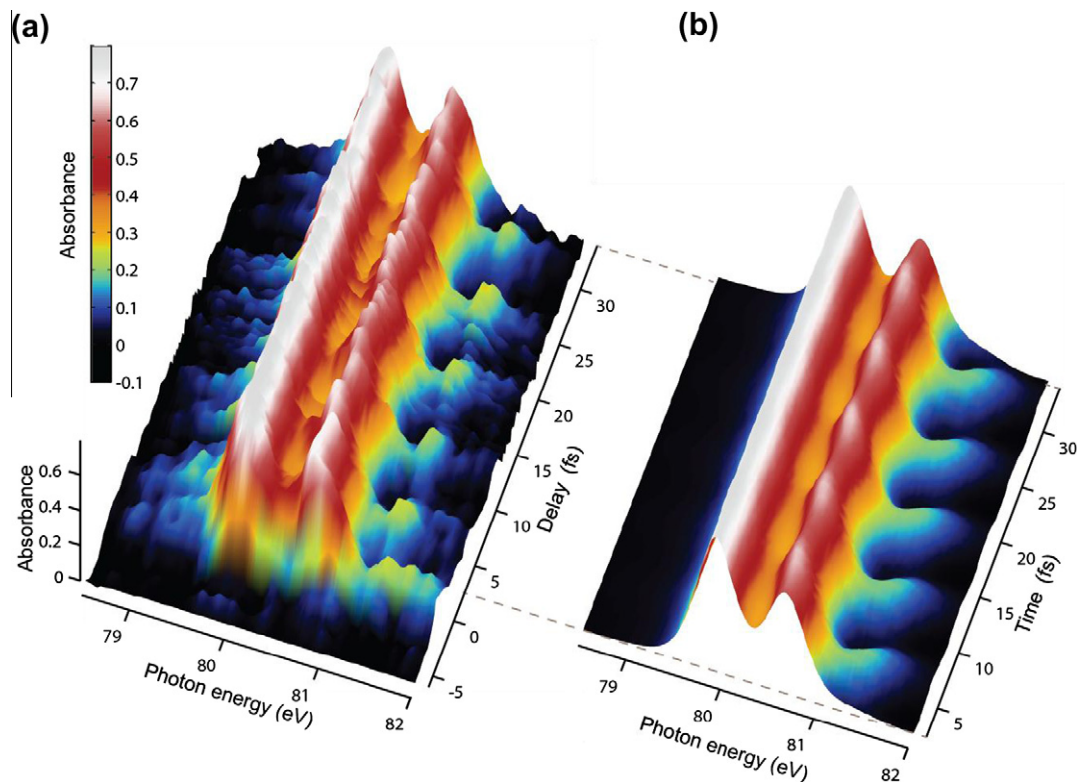


Fig. 6. Real-time tracing of electron coherences in singly-charged krypton ions and its model fit. (a) Measured attosecond transient absorption spectrogram, recording the dynamic absorbance over an extended delay range (14.1–24.0 fs) with a step of 1 fs and including a delay range where the sampling resolution has been increased to 0.3 fs. The fit of the data based on our modeling limited to the NIR field free delay range ($\tau > 3$ fs), contrasts the measurement (b).

quantity δ equals the initial quantum phase. We fit the data set by employing the Levenberg–Marquardt optimization algorithm in the range 78.5–82 eV and for the delays exceeding 3 fs in order to avoid the buildup of the populations of the ionic states which is not taken into account by our reconstruction routine. The fit parameters are the populations ($\rho_{1/2,1/2}^{(1/2)}, \rho_{3/2,3/2}^{(1/2)}, \rho_{3/2,3/2}^{(3/2)}$), the terms describing the coherence ($|\rho_{3/2,1/2}^{(1/2)}|, \Delta E_{SO}, \delta$), the three central energies of the EUV transitions ($E_{3d_{5/2}} - E_{4p_{3/2}}, E_{3d_{3/2}} - E_{4p_{3/2}}, E_{3d_{3/2}} - E_{4p_{1/2}}$), as well as the spectrometer resolution Δ and the constant offset A_0 .

The populations provided are scaled to 100% fractional ionization after the fitting procedure.

The best fit to the measured data set is shown in Fig. 6(b). We retrieve the normalized populations $\rho_{3/2,3/2}^{(\pm 1/2)} = 0.446 \pm 0.069$, $\rho_{1/2,1/2}^{(\pm 1/2)} = 0.37 \pm 0.024$, and $\rho_{3/2,3/2}^{(\pm 3/2)} = 0.184 \pm 0.075$, the coherence $\rho_{3/2,1/2}^{(1/2)} = 0.1092 \pm 0.0071$, which results in a degree of coherence $\gamma = 0.538 \pm 0.070$ and an alignment $\Theta = 0.42 \pm 0.17$. The retrieved spin–orbit wavepacket period amounts to $T_{(SO)} = 6.338 \pm 0.028$ fs.

This complete experimental characterization of the quantum mechanical electron motion, described with a reduced density matrix, based on the measured attosecond transient absorption spectrogram enables—along with appropriate modeling—the visualization of the electron motion inside the Kr^+ valence shell. To reconstruct the quantum mechanical motion of the electron wavepacket for every sampled snapshot, the temporal evolution of the quantum phase $\varphi_{SO}(\tau)$ must also be retrieved. Attosecond absorption spectroscopy allows this retrieval over a multi-femtosecond time interval with attosecond resolution. Fig. 7(a) displays the mean optical density of the $4p_{3/2}^{-1} \rightarrow 3d_{3/2}^{-1}$ absorption line as a function of pump–probe delay over the energy range 81.20–81.45 eV (black dots) for the scan shown in Fig. 6(a), focused at the interval which had been sampled at a high resolution ($\Delta\tau = 300$ as). This is contrasted with the prediction of our model

for the fit parameters given above (full line). The blue dots show the evolution of the retrieved quantum phase at each sampled delay. Error bars are smaller than $\pm\pi/15$. This allows the rigorous reconstruction of the hole-density distribution at any instant after the ionizing laser pulse with subfemtosecond accuracy. Results of this reconstruction at a few selected instances separated by 600 as and spanning approximately half a spin–orbit wavepacket period, are plotted in Fig. 7(b), starting at $t = 17.1$ fs as indicated by the red arrow in panel (a). The six panels show the evolution of the hole density $Q(r, \theta, t)$ as tomographic cross-cuts through the center of the 3D distribution for reconstructed density matrix elements. For plotting these tomographic cuts, the angular hole density distribution $h(\theta, t)$ had been multiplied with the radial part $\rho(r)$ of the wavefunction defined in Eq. (44) of [46]. As indicated earlier the hole density is cylindrically symmetric around the quantization axis (z -axis) and therefore depends on the radius r , the elapsed time t and the polar angle θ . The Kr 4p orbital underlying this density has been calculated using the Hartree–Slater method implemented by Herman and Skillman [51]. The chosen color map is optimized to highlight the dynamics.

4.3. Tracing coherences in doubly ionized atoms—studying correlated double hole systems in the time domain

Does a strong field trigger fast electron wavepacket dynamics in doubly charged ions? From a fundamental point of view, the multiplet structure of Kr^{2+} is determined by spin–orbit coupling (like in Kr^+) and in addition by hole–hole Coulomb interactions. To theoretically address such systems in the time domain by ab initio multichannel methods is a rather challenging task. Our experimental methodology offers the possibility of a first glimpse into the dynamics of such systems. Fig. 8 displays the same absorption spectrogram

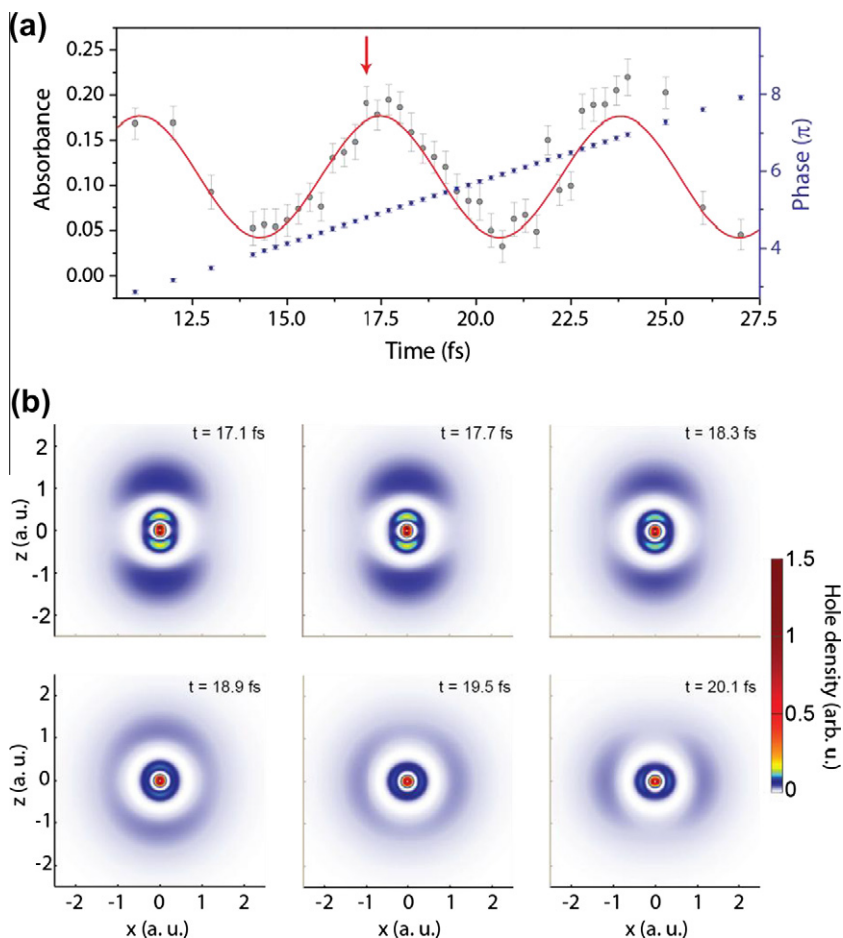


Fig. 7. Complete reconstruction of valence electron density. (a) Integrated experimental absorbance in the range 81.25–81.53 eV of the $4p_{3/2}^{-1} \rightarrow 3d_{3/2}^{-1}$ absorption line. Full line shows the result of our modeling for the values of the fit parameters given in the text. Error bars depict standard errors. Reconstruction of the quantum phase between the $J = 3/2$, $M_J = \pm 1/2$ and $J = 1/2$, $M_J = \pm 1/2$ states. (b) Complete reconstruction of the electronic hole density in arbitrary units (arb.u.) displayed as spatial-tomographic cross-sections through the ion (z -axis denotes axis of NIR polarization). Snapshots are displayed for every second adjacently sampled absorption spectrum starting at $\tau = 17.1$ fs (indicated by red mark in (a)), spaced by 0.6 fs. Spatial dimensions in atomic units (a.u.).

as in Fig. 6(a), plotted over a broader spectral range (78–85 eV) to allow access into absorption dynamic of the Kr^{2+} ion (at 83 eV).

At first glance, the temporal evolution of the strength of the absorption lines—associate to the doubly charged krypton ions—does not exhibit any obvious periodic modulations. To further investigate this, we perform a fast Fourier transformation (FFT) along the time axis (2.5 up to 34.5 fs). Constant offsets in the absorbance along the energy axis of Fig. 8, are subtracted before FFT is applied. The natural logarithm of the spectral intensity as a function of photon energy and beating frequency (represented as energy) is displayed in Fig. 9 for frequencies lower than the Nyquist (~ 6.9 eV). The pronounced beating frequency of ~ 0.66 eV primarily detected at the spectral range where Kr^+ lines are dominant (see left panel)—corresponds well to the spin-orbit wavepacket dynamics in the singly charged ion as discussed in the previous section.

Fig. 10(a) shows binned and averaged spectral intensity derived by FFT in the energy range of 82.3–85 eV, thus covering most of the resonant transitions of the doubly charged ions (see Fig. 4). Electronic configurations that include only a few excited levels of Kr^{2+} [48] Fig. 10(b), are sufficient for the assignment of the experimentally observed beating frequencies—shown as vertical lines—to various pairs of excited Kr^{2+} states marked by a \otimes . Frequencies below ~ 0.25 eV are sensitive to background subtraction methods and are therefore omitted from this study. It is clear from the energy diagram of Fig. 10(b) that superpositions among the first triplet P states and the singlet D state with the triplet P states seem to explain most of the observed quantum beats.

Faster electronic dynamics are likely to suffer a reduced coherence due to the extended ionization gate of the few-cycle pulse compared to their characteristic period of oscillation.

The data of Fig. 10 offers therefore clear evidence that a doubly charged krypton ion undergoes a more complex wavepacket motion which involves two holes generated by the strong field. The fastest quantum motion which is observed is the coherent superposition of the singlet D state and the 3P_2 state at a frequency of 1.82 eV corresponding to a period of 2.27 fs.

The observation of quantum beats, resulting from superpositions involving triplet P states and the singlet D state, indicates that strong-field ionization by a ~ 3.8 fs NIR laser pulse creates doubly charged ions not only in their ground state, but also in higher excited states. Applying the most naive tunneling picture, the NIR field is expected to ionize the two $4p_z$ electrons (z -axis is the quantization axis aligned with the laser polarization) [45,52]. The corresponding two-hole wavepacket would then be a superposition of the two-hole singlet D and singlet S states. Based on this perspective and in contrast to the measurement, one would only expect the beating frequency at 2.29 eV to appear. The current observation of beats however indicates that coherent superpositions are even arising between triplet P states, which are inconsistent with the simplified tunneling picture. Here we can conclude that not only the D and S states of Kr^{2+} are populated, but also the P state manifold and that strong-field ionization even prepares them in a coherent superposition state. Further experiments, to be performed with higher sampling resolution and longer scan ranges,

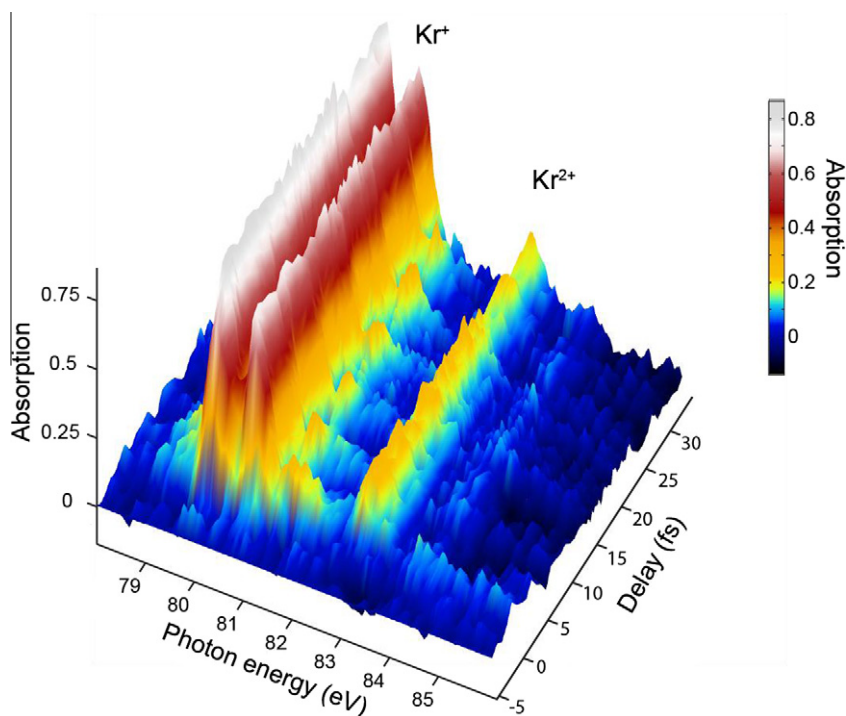


Fig. 8. Tracing electronic dynamics in doubly charged krypton ions. The strongest absorption line of Kr^{2+} can be related to the manifolds of states pertinent to the $4p^{-2}3P_2 \rightarrow 3d^{-1}4p^{-1}$ transition.

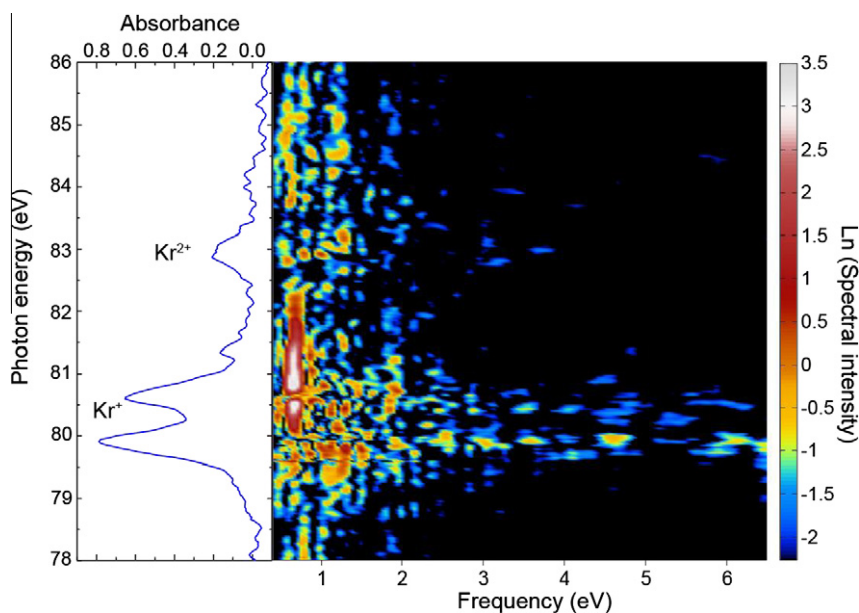


Fig. 9. FFT retrieval of ultrafast coherences in Kr^{2+} ions. Spectral intensity of a fast Fourier transformation of the attosecond transient absorption spectrogram shown in Fig. 8, limited to the NIR field-free delay range extending from 2.5 to 34.5 fs. Graph on the left side is an absorption spectrum binned over the delay values 30–34.5 fs of the data of Fig. 8.

will increase the resolution in the frequency domain and will offer the potential of more detailed studies on double hole—and potentially even triple hole—dynamics in the future.

4.4. Electronic coherences in xenon ions

We have also taken first steps in studying ultrafast dynamics in heavier atoms like Xe. In particular, we investigate strong-field ionized xenon atoms at an NIR intensity of $(3.1 \pm 0.5) \cdot 10^{14} \text{ W/cm}^2$ (Fig. 11). Owing to the lower ionization potential of xenon

compared to that of krypton, the emergence of several charge states is to be expected at this intensity.

For positive delays—EUV follows the NIR pulse—the trace shows a build-up of discrete absorption structures as well as spectrally broad absorption features which are created by resonant (close to the continuum) and nonresonant (into continuum) EUV absorption. A strong absorption line at $\sim 87.8 \text{ eV}$ is the dominant feature; absorption lines with conspicuous modulation as a function of the delay are present both at the higher as well as at lower energies with respect to this resonance. Some of the observed coherences

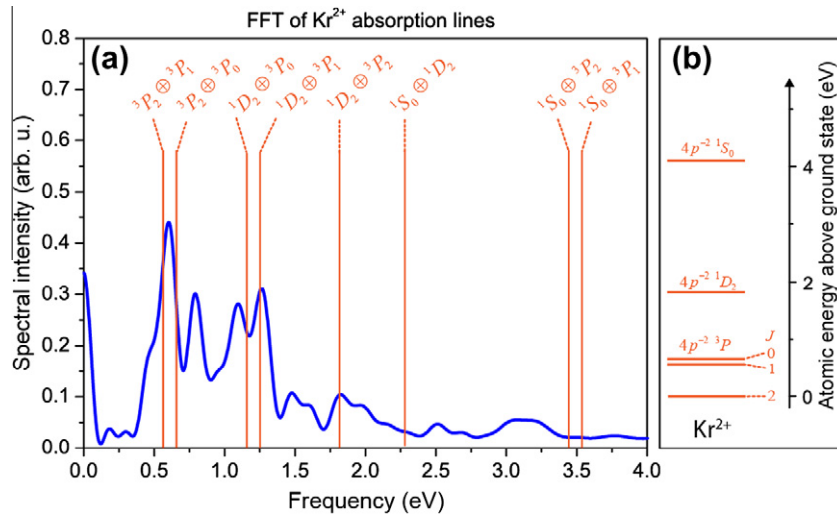


Fig. 10. Double-hole dynamics in Kr²⁺. (a) Binned and averaged lineout of the FFT shown in Fig. 9, over the absorption range of Kr²⁺ ions (82.3–85 eV). Beating frequencies between pairs of states—according to the energy diagram of (b)—are denoted by ⊕ and are marked as vertical lines. (b) Energy level diagram of Kr²⁺, limited to the first few excited states above the ground state [48].

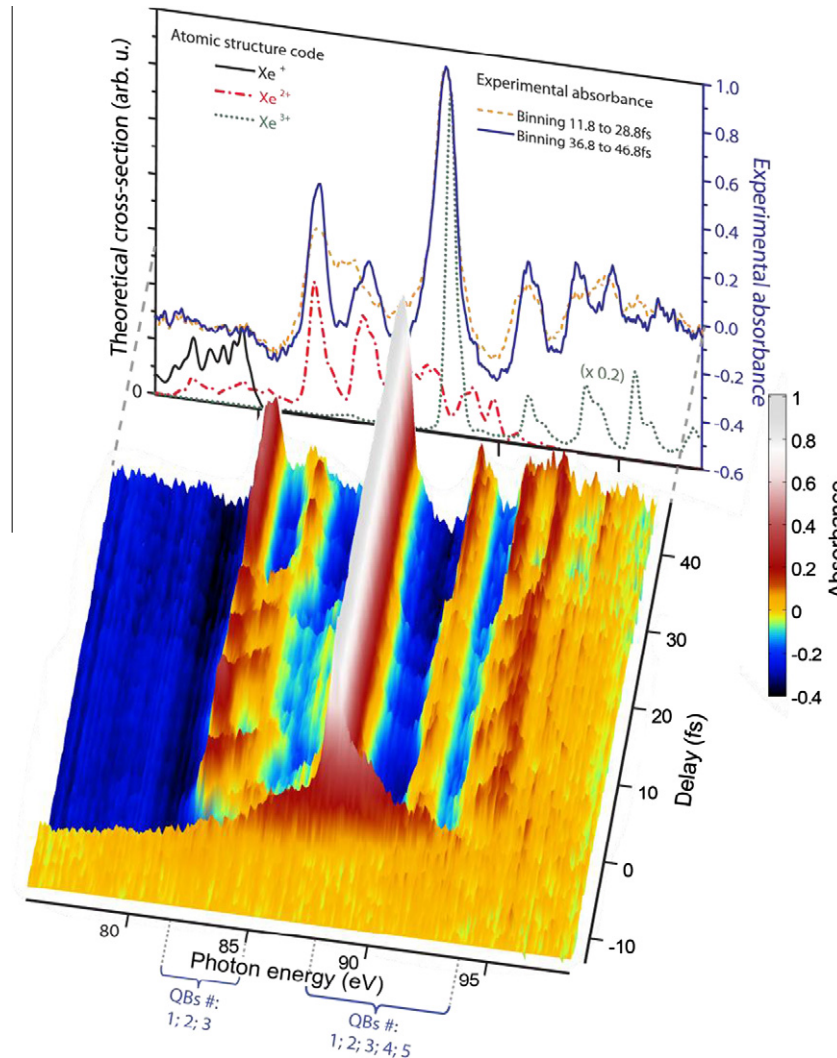
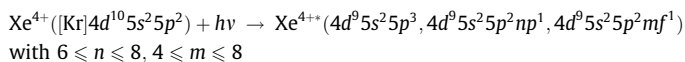
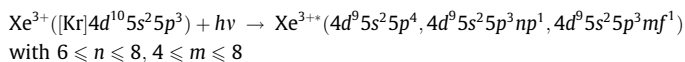
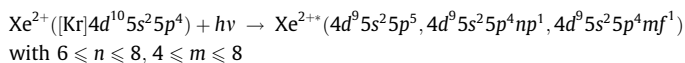
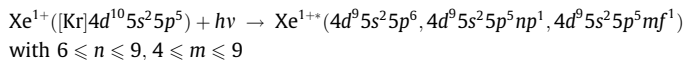


Fig. 11. Attosecond transient absorption spectrogram obtained in xenon. Neutral atoms were strong-field ionized by quasi-monocycle NIR laser pulses at $\sim 5 \cdot 10^{14}$ W/cm². The time dependent absorbance topography comprises multiple quantum beats and a spectrally broad area of negative absorbance. The spectrum in the background compares calculated electric dipole spectra. The blue curve displays the averaged absorbance in the range 36.8–44.8 fs and the dashed orange curve the averaged experimental absorbance averaged over the delay range 11.8–28.8 fs. Quantum beats observed in the two spectral windows as indicated at the bottom of the figure name quantum beat numbers (QB#) for which superimposed state pairs and their energy difference are contained in Table 1.

exhibit aperiodic oscillations, indicating periodicities being longer than the scanning range. Besides a gradual increase of the absorption for the resonant lines at positive delays, a spectrally broad increase of transmission (negative absorption) is observed at photon energies below 92 eV. To identify the main contributions in the recorded spectra we have followed similar methods as introduced in the previous sections. The graph in the background of Fig. 11 compares calculated absorption cross-section for singly, doubly and triply ionized xenon within experimental spectra sampled at a delay of 38 fs. The shown spectra are obtained by electronic structure calculations considering the following initial and final electron configuration:



where several hundreds of levels are added up incoherently for one charge state. The major discrete resonant lines of Xe^+ are located well below 75 eV. The transition from the 4d level to low-lying ionic Xe Rydberg states are located within the experimentally observed spectral range for the ions Xe^{2+} and Xe^{3+} and only marginally for Xe^+ . An explanation of the formation of the coherences based on potential superpositions within the $5s^25p^4$ and the $5s^15p^5$ electron configuration of Xe^{2+} fails. Moreover, the appearance of very similar frequencies imprinted on the absorption lines of Xe^{3+} supports a different source of the quantum motion [53]. A preliminary, but rather promising approach of unveiling the origin of the coherences is to assign the beats to electron motion in the excited singly charged ion as they absorb in the same spectral range where Xe^{2+} exhibits absorption lines. An excited Xe^+ ion would comprise a Xe^{2+} -like core and a Rydberg electron such that low-lying absorption resonances resemble Xe^{2+} resonances, being perturbed by the Rydberg electron. Similarly, an excitation of the Xe^+ ion into an autoionizing state where two Rydberg electrons are launched during the strong-field ionization event would yield a Xe^{3+} core. In fact, some measured beating frequencies can be assigned to superposition state pairs of excited Xe^+ . Pronounced beating frequencies in the spectral range 82.1–85 eV (Xe^{2+}) and 87.2–93.0 eV (Xe^{3+}) are labeled with QB-numbers (QB#) as indicated in Fig. 11. Table 1 lists pairs of quantum states that correspond to the observed quantum beat frequencies [54].

The fast frequencies appearing on the Xe^{3+} lines at ~ 0.25 and ~ 1.6 eV are in good agreement with coherent population of states of the triply charged ion. Here we can preliminarily conclude that strong-field created Xe^{3+} ions are coherently populated within the $5s^25p^3$ manifold of states. Thus, the experimental observation supports the linear superposition in $5s^25p^3$ of ${}^3P_{1/2}$ and ${}^3D_{5/2}$ and of ${}^2D_{3/2}$ and ${}^4S_{3/2}$ in this ion. The latter coherently populated state pair infers a spin-orbit wavepacket period of ~ 2.5 fs which probably approaches the limit of fastest electronic motion that can be efficiently triggered with quasi monocycle NIR pulses but however does not mark a limitation of the employed attosecond-EUV probing scheme.

Table 1

List of quantum state pairs that correspond to observed electronic coherences in xenon ions. The peak no. references the superposition state pairs to the observed beating signatures as marked in Fig. 11.

Peak no.	ΔE (eV)	Ionic system	Superposition state pairs
1	~ 0.27	Xe^+ Xe^+	$\{5s5p^6 {}^2S_{1/2}; 5s^25p^4 ({}^3P_2)6s^2 [2]_{5/2}\}$ $\{5s^25p^4 ({}^3P_2)6s^2 [2]_{3/2}; 5s^25p^4 ({}^3P_2)6s^2 [2]_{5/2}\}$
2	~ 0.47	Xe^+ Xe^+	$\{5p^4 ({}^3P_2)5d^2 [1]_{1/2}; 5s^25p^4 ({}^3P_2)6s^2 [2]_{5/2}\}$ $\{5p^4 ({}^3P_2)5d^2 [4]_{7/2}; 5p^4 ({}^3P_2)5d^2 [1]_{3/2}\}$
3	0.79	Xe^+	$\{5p^4 ({}^3P_2)5d^2 [4]_{9/2}; 5p^4 ({}^3P_2)6s^2 [2]_{5/2}\}$
4	1.31	Xe^{3+}	$\{5s^25p^3 {}^3P_{1/2}; 5s^25p^3 {}^3D_{5/2}\}$
5	1.64	Xe^{3+}	$\{5s^25p^3 {}^2D_{3/2}; 5s^25p^3 {}^4S_{3/2}\}$

4.5. Ultrafast depletion of neutral Xe atoms

The observed broad negative absorbance, particularly for energies <92 eV, suggests an NIR induced increase of the EUV transmission by 35% following the NIR pulse. It can be attributed to the difference in the photoabsorption cross-section between various charge states [55] particularly between the strong field depleted neutral Xe and the generated ions. Similarly to the resonant case the evolution of the transmittance tracks the difference in the population dynamics between different charge states in the strong light field.

5. Conclusions

We have introduced attosecond transient absorption spectroscopy, a novel probing technique for tracing ionization dynamics as well as valence shell electronic coherences in real time. Our approach extends real-time measurements from nuclear dynamics and Rydberg electron dynamics to motion confined in the valence shell of ions and opens up new perspectives for control on the nanoscale. Tracing the creation of ions by the strong field, has permitted a real-time observation of the sub-cycle delay in the formation between different charge states. Thanks to the ultrafast ionization gate generated by our quasi-monocycle laser pulse, coherent spin-orbit wavepacket motion in the valence shell of Kr^+ with a high degree of coherence has been triggered. The unfolding dynamics of the valence electron density is traced by the attosecond EUV pulse, which for the first time is placed at the role of the probe. Recent efforts [38] employing a synthesized sub-optical pulse have succeeded the demonstration of sub-fs triggering and have extended this technique to be an attosecond pump probe scheme for capturing valence shell coherences in virtually any microscopic system. Precise modeling enables the complete reconstruction of the evolving valence electron motion as a function of pump-probe delay, including its degree of coherence.

Beyond this proof-of-concept experiment, attosecond transient absorption spectroscopy has been used to trace electron dynamics in more complex systems such as Kr^{2+} and Xe ions. In particular we have observed coherent electron motion in Kr^{2+} with an oscillating period as fast as 2.3 fs. These results hold promise for detailed time domain studies of hole-hole and multi-hole correlations in atoms and molecules, making attosecond transient absorption spectroscopy an ideal tool for testing the currently available theoretical understanding of such systems as well as for supporting advanced applications on the nanoscale.

Acknowledgements

We acknowledge the development of dedicated attosecond soft X-ray optics by Michael Hofstetter and Ulf Kleineberg (LMU, MPQ)

and are grateful for the invaluable contributions of Zhi-Heng Loh, Nina Rohringer, Vladislav S. Yakovlev, Matthias F. Kling, Markus Fieß, Thomas Pfeifer, Sergey Zherebtsov, Abdallah M. Azzeer, Stephen R. Leone and Ferenc Krausz. This work was supported by the Max Planck Society, the European Research Council Grant (Attoelectronics-258501), the DFG Cluster of Excellence: Munich Centre for Advanced Photonics (www.munich-photonics.de) and the King Saud University-MPQ collaboration. R.S. acknowledges support by the Deutsche Forschungsgemeinschaft (DFG) under Grant No. SFB 925/A5.

References

- [1] F. Krausz, M. Ivanov, *Rev. Mod. Phys.* 81 (2009) 163.
- [2] E. Goulielmakis, V.S. Yakovlev, A.L. Cavalieri, M. Uiberacker, V. Pervak, A. Apolonski, R. Kienberger, U. Kleineberg, F. Krausz, *Science* 317 (2007) 769.
- [3] A. Baltuska, T. Udem, M. Uiberacker, M. Hentschel, E. Goulielmakis, C. Gohle, R. Holzwarth, V.S. Yakovlev, A. Scrinzi, T.W. Hansch, F. Krausz, *Nature* 422 (2003) 189.
- [4] J. Itatani, F. Quéré, G.L. Yudin, M.Y. Ivanov, F. Krausz, P.B. Corkum, *Phys. Rev. Lett.* 88 (2002) 173903.
- [5] R. Kienberger, E. Goulielmakis, M. Uiberacker, A. Baltuska, V. Yakovlev, F. Bammer, A. Scrinzi, T. Westerwalbesloh, U. Kleineberg, U. Heinzmann, M. Drescher, F. Krausz, *Nature* 427 (2004) 817.
- [6] E. Goulielmakis, M. Uiberacker, R. Kienberger, A. Baltuska, V. Yakovlev, A. Scrinzi, T. Westerwalbesloh, U. Kleineberg, U. Heinzmann, M. Drescher, F. Krausz, *Science* 305 (2004) 1267.
- [7] G. Sansone, E. Benedetti, F. Calegari, C. Vozzi, L. Avaldi, R. Flammini, L. Poletto, P. Villoresi, C. Altucci, R. Velotta, S. Stagira, S. De Silvestri, M. Nisoli, *Science* 314 (2006) 443.
- [8] E. Goulielmakis, M. Schultze, M. Hofstetter, V.S. Yakovlev, J. Gagnon, M. Uiberacker, A.L. Aquila, E.M. Gullikson, D.T. Attwood, R. Kienberger, F. Krausz, U. Kleineberg, *Science* 320 (2008) 1614.
- [9] S. Gilbertson, S.D. Khan, Y. Wu, M. Chini, Z. Chang, *Phys. Rev. Lett.* 105 (2010) 093902.
- [10] V.S. Yakovlev, J. Gagnon, N. Karpowicz, F. Krausz, *Phys. Rev. Lett.* 105 (2010) 073001.
- [11] M. Ivanov, O. Smirnova, *Phys. Rev. Lett.* 107 (2011) 213605.
- [12] M. Schultze, M. Fieß, N. Karpowicz, J. Gagnon, M. Korbman, M. Hofstetter, S. Neppl, A.L. Cavalieri, Y. Komninos, T. Mercouris, C.A. Nicolaides, R. Pazourek, S. Nagele, J. Feist, J. Burgdörfer, A.M. Azzeer, R. Ernstorfer, R. Kienberger, U. Kleineberg, E. Goulielmakis, F. Krausz, V.S. Yakovlev, *Science* 328 (2010) 1658.
- [13] G. Sansone, F. Kelkensberg, J.F. Perez-Torres, F. Morales, M.F. Kling, W. Siu, O. Ghafur, P. Johnsson, M. Swoboda, E. Benedetti, F. Ferrari, F. Lepine, J.L. Sanz-Vicario, S. Zherebtsov, I. Znakovskaya, A. L'Huillier, M.Y. Ivanov, M. Nisoli, F. Martin, M.J.J. Vrakking, *Nature* 465 (2010) 763.
- [14] A.L. Cavalieri, N. Muller, T. Uphues, V.S. Yakovlev, A. Baltuska, B. Horvath, B. Schmidt, L. Blumel, R. Holzwarth, S. Hendel, M. Drescher, U. Kleineberg, P.M. Echenique, R. Kienberger, F. Krausz, U. Heinzmann, *Nature* 449 (2007) 1029.
- [15] F. Remacle, M. Nest, R.D. Levine, *Phys. Rev. Lett.* 99 (2007) 183902.
- [16] J. Mauritsson, T. Remetter, M. Swoboda, K. Klünder, A. L'Huillier, K.J. Schafer, O. Ghafur, F. Kelkensberg, W. Siu, P. Johnsson, M.J.J. Vrakking, I. Znakovskaya, T. Uphues, S. Zherebtsov, M.F. Kling, F. Lépine, E. Benedetti, F. Ferrari, G. Sansone, M. Nisoli, *Phys. Rev. Lett.* 105 (2010) 053001.
- [17] O. Smirnova, Y. Mairesse, S. Patchkovskii, N. Dudovich, D. Villeneuve, P. Corkum, M.Y. Ivanov, *Nature* 460 (2009) 972.
- [18] S. Haessler, J. Caillat, W. Boutu, C. Giovanetti-Teixeira, T. Ruchon, T. Auguste, Z. Diveki, P. Preger, A. Maquet, B. Carre, R. Taieb, P. Salieres, *Nat. Phys.* 6 (2010) 200.
- [19] A. Fleischer, H.J. Wörner, L. Arissian, L.R. Liu, M. Meckel, A. Rippert, R. Dörner, D.M. Villeneuve, P.B. Corkum, A. Staudte, *Phys. Rev. Lett.* 107 (2011) 113003.
- [20] G.A. Worth, L.S. Cederbaum, *Annu. Rev. Phys. Chem.* 55 (2004) 127.
- [21] D.C. Koningsberger, R. Prins, *X-ray Absorption: Principles, Applications, Techniques of EXAFS, SEXAFS and XANES*, John Wiley & Sons Inc., New York, 1987.
- [22] F. de Groot, *Chem. Rev.* 101 (2001) 1779.
- [23] P.A. Lee, P.H. Citrin, P. Eisenberger, B.M. Kincaid, *Rev. Mod. Phys.* 53 (1981) 769.
- [24] E. Seres, J. Seres, C. Spielmann, *Appl. Phys. Lett.* 89 (2006) 181919.
- [25] Z.H. Loh, M. Khalil, R.E. Correa, R. Santra, C. Buth, S.R. Leone, *Phys. Rev. Lett.* 98 (2007).
- [26] Z.-H. Loh, S.R. Leone, *J. Chem. Phys.* 128 (2008) 204302.
- [27] H. Wang, M. Chini, S. Chen, C.-H. Zhang, F. He, Y. Cheng, Y. Wu, U. Thumm, Z. Chang, *Phys. Rev. Lett.* 105 (2010) 143002.
- [28] M. Holler, F. Schapper, L. Gallmann, U. Keller, *Phys. Rev. Lett.* 106 (2011) 123601.
- [29] M. Jurvansuu, A. Kivimaki, S. Aksela, *Phys. Rev. A* 64 (2001).
- [30] W.T. Pollard, R.A. Mathies, *Annu. Rev. Phys. Chem.* 43 (1992) 497.
- [31] W.T. Pollard, S.-Y. Lee, R.A. Mathies, *J. Chem. Phys.* 92 (1990) 4012.
- [32] R. Mathies, C. Brito Cruz, W. Pollard, C. Shank, *Science* 240 (1988) 777.
- [33] Q. Wang, R. Schoenlein, L. Peteanu, R. Mathies, C. Shank, *Science* 266 (1994) 422.
- [34] M. Schultze, A. Wirth, I. Grguras, M. Uiberacker, T. Uphues, A.J. Verhoef, J. Gagnon, M. Hofstetter, U. Kleineberg, E. Goulielmakis, F. Krausz, *J. Electron. Spectrosc.* 184 (2011) 68.
- [35] Y. Mairesse, F. Quere, *Phys. Rev. A* 71 (2005) 1.
- [36] J. Gagnon, E. Goulielmakis, V.S. Yakovlev, *Appl. Phys. B* 92 (2008) 25.
- [37] M. Sher, *Proc. SPIE* 1860 (1993) 112.
- [38] A. Wirth, M.T. Hassan, I. Grguraš, J. Gagnon, A. Moulet, T.T. Luu, S. Pabst, R. Santra, Z.A. Alahmed, A.M. Azzeer, V.S. Yakovlev, V. Pervak, F. Krausz, E. Goulielmakis, *Science* 334 (2011) 195.
- [39] C. McGuinness, Robert D. Cowan's atomic structure code, 2007. Available from: <<http://www.tcd.ie/Physics/People/Cormac.McGuinness/Cowan/>>.
- [40] R.D. Cowan, *The Theory of Atomic Structure and Spectra*, University of California Press Ltd., London, 1981.
- [41] O.P. Sairanen, A. Kivimaki, E. Nommiste, H. Aksela, S. Aksela, *Phys. Rev. A* 54 (1996) 2834.
- [42] S.H. Autler, C.H. Townes, *Phys. Rev.* 100 (1955) 703.
- [43] L. Young, D.A. Arms, E.M. Dufresne, R.W. Dunford, D.L. Ederer, C. Hohl, E.P. Kanter, B. Krassig, E.C. Landahl, E.R. Peterson, J. Rudati, R. Santra, S.H. Southworth, *Phys. Rev. Lett.* 97 (2006).
- [44] H. Rottke, J. Ludwig, W. Sandner, *J. Phys. B At. Mol. Opt. Phys.* 29 (1996) 1479.
- [45] E. Gubbini, U. Eichmann, M. Kalashnikov, W. Sandner, *Phys. Rev. Lett.* 94 (2005).
- [46] N. Rohringer, R. Santra, *Phys. Rev. A* 79 (2009) 053402.
- [47] F.A. Parpia, C.F. Fischer, I.P. Grant, *Comp. Phys. Commun.* 94 (1996) 249.
- [48] E.B. Saloman, *J. Phys. Chem. Ref. Data* 36 (2007) 215.
- [49] E. Goulielmakis, Z.-H. Loh, A. Wirth, R. Santra, N. Rohringer, V.S. Yakovlev, S. Zherebtsov, T. Pfeifer, A.M. Azzeer, M.F. Kling, S.R. Leone, F. Krausz, *Nature* 466 (2010) 739.
- [50] R. Santra, V.S. Yakovlev, T. Pfeifer, Z.-H. Loh, *Phys. Rev. A* 83 (2011) 033405.
- [51] F. Herman, S. Skillman, *Atomic Structure Calculations*, Prentice-Hall, New York, 1963.
- [52] R. Taieb, V. Veniard, A. Maquet, *Phys. Rev. Lett.* 87 (2001).
- [53] A. Wirth, *Attosecond Transient Absorption Spectroscopy*, Ph.D. thesis, Faculty of Physics, Ludwig Maximilians University of Munich, 2011.
- [54] E.B. Saloman, *J. Phys. Chem. Ref. Data* 33 (2004) 765.
- [55] T. Koizumi, Y. Awaya, A. Fujino, Y. Itoh, M. Kitajima, T.M. Kojima, M. Oura, R. Okuma, M. Sano, T. Seikioka, N. Watanabe, F. Koike, *Phys. Scr.* T73 (1997) 131.